

# Spatiotemporal Cooperative Effect Between the Time-asymmetric Ratio of Oscillating Trailing Edge Flap and Pivot Location on the Aerodynamics of a Pitching Airfoil

L. Zhu<sup>1</sup>, R. Guo<sup>1†</sup>, Z. Lai<sup>2</sup>, L. Qi<sup>1</sup>, and C. Yin<sup>1</sup>

<sup>1</sup> School of Mechanical Engineering, Guizhou University, Guiyang, Guizhou, 550025, China

<sup>2</sup> Zhejiang Laboratory, Hangzhou, Zhejiang, 311121, China

†Corresponding Author Email: [rxguo@gzu.edu.cn](mailto:rxguo@gzu.edu.cn)

## ABSTRACT

The time-asymmetric ratio ( $\delta$ ) of an oscillating trailing edge flap (TEF) significantly affects the aerodynamics of a pitching airfoil at low Reynolds numbers and its associated complex flow features. This study aims to investigate how variations in  $\delta$  influence the lift and drag coefficients for fixed-pivot configurations. Numerical simulations indicate that increasing  $\delta$  enhances lift during the upstroke, and accelerates flow development. This occurs because  $\delta$  fundamentally modifies the growth rates of various vortices, directly affecting the pressure distribution on the airfoil surface. The study also examines the impact of pivot location ( $x_p/c$ ) on aerodynamic performance and vortex structures at  $\delta = 0$ . Results reveal that moving the pivot location backward delays flow evolution without improving lift. A detailed assessment of  $\delta$  and  $x_p/c$  highlights the spatiotemporal cooperative effect, leading to the proposal of new definitions for the effective angle of attack to these interactions. At a dimensionless number  $Z = 0.008$ , setting  $\delta$  to  $\pm 0.1$  quantitatively replicates the effect of a forward or backward pivot, shift equivalent to  $0.25c$ . These findings offer valuable insights into the simplified control of airfoil kinematics for achieving exceptional maneuverability and serve a reference for the design of the new flapping machines.

## Article History

Received November 14, 2024

Revised January 25, 2025

Accepted February 13, 2025

Available online May 5, 2025

## Keywords:

Lift augmentation

Pivot location

Spatiotemporal cooperative effect

Time-asymmetric ratio

Trailing edge flap

## 1. INTRODUCTION

Flapping flight has demonstrated that appropriate unsteady airfoil motions significantly enhance lift characteristics, improve locomotion stability, and enable extraordinary maneuvers observed in natural flyers and bioinspired propulsors within a Reynolds number range of  $10^3$  to  $10^5$ . Independent or combined motions of pitching and plunging (Kim & Chang, 2014; Moriche et al., 2017; Akoz et al., 2021) have been shown to maximize lift and thrust. Key factors influencing aerodynamics include amplitude (Bull et al., 2021), reduced frequency (Majumdar et al., 2022), and phase shift (Elfering & Granlund, 2020) between different motion types.

The time-asymmetric ratio, defined as the difference between upstroke and downstroke durations within a motion period, remains less understood despite its frequent occurrence in the flapping motions of natural flyers for locomotion enhancement. Experimental (Wang et al., 2021) and computational studies (Lu et al., 2013; Chen et al., 2022) indicated that the time-asymmetric ratio

enhanced force generation, strengthened vorticity, and accelerated flow. A higher time-asymmetric ratio induces a stronger reverse von Karman vortex in the wake, leading to increased thrust. Thakor et al. (2020) reported that the time-asymmetric ratio in pitching strokes significantly influenced vortex pair formation and braid strength. Chao et al. (2021) further demonstrated that wake structures composed of paired and single vortices generated both drag and thrust under time-asymmetric oscillation.

However, there is a performance enhancement threshold at high angles of attack, particularly in the dynamic stall regime. Enhancing flapping capabilities often necessitates deformable structures. Trailing edge flaps (TEFs) have been proven effective (Lu et al., 2017), as the increased maximum lift is attributed to positive camber effects (Gerontakos & Lee, 2008; Fernandez-Feria & Alaminos-Quesada, 2021). Seamless, flexible TEF deformations delay stall by altering vortex-shedding patterns (Kan et al., 2020; Shi et al., 2020; Hao et al., 2021; Jawahar et al., 2022). Inspired by optimized body

| NOMENCLATURE |                                 |                       |   |
|--------------|---------------------------------|-----------------------|---|
| $c$          | chord length                    | $T$                   | duration of an oscillating cycle                            |
| $f$          | pitching frequency              | $U_\infty$            | freestream velocity   |
| $h$          | plunging distance               | $Z$                   | speed ratio of predominant pitching motion                  |
| $h_0$        | plunging amplitude              | $\alpha$              | angle of attack   |
| $k$          | reduced frequency               | $\alpha_0$            | original angle of attack                                    |
| $t_d$        | duration of downward deflection | $\alpha_h$            | induced angle of attack by plunging motion                  |
| $t_u$        | duration of upward deflection   | $\alpha_m$            | pitching amplitude  |
| $x_p/c$      | pivot location                  | $\alpha_{eff}^\delta$ | effective angle of attack considering time-asymmetric ratio |
| $C_L$        | lift coefficient                | $\alpha_{eff}^p$      | effective angle of attack considering pivot location        |
| $C_D$        | drag coefficient                | $\beta$               | deflecting angle  |
| $C_p$        | pressure coefficient            | $\beta_0$             | oscillating amplitude                                       |
| $\bar{C}_L$  | averaged lift coefficient       | $\delta$              | time-asymmetric ratio                                       |
| $\bar{C}_D$  | averaged drag coefficient       | $\omega$              | angular frequency   |
| $Re$         | Reynolds number                 | $\Delta t$            | time step   |

movements, morphing airfoils with trailing-edge adaptations have become a critical research focus. Akhter et al. (2022) demonstrated that spanwise morphing facilitated boundary layer reattachment, thereby increasing lift. Wu et al. (2023) employed phase-shifted trailing-edge morphing to suppressed stall flutter amplitude in limit-cycle oscillations, identifying a phase of  $\pi/2$  as optimal for lift production. Movable TEFs are thus utilized for active flow control, enhancing lift without significantly increasing drag (Ting et al., 2018; Govindan et al., 2023). From the perspective of flow mechanism, oscillating TEFs influence the development of laminar separation bubbles on the suction side (Mohamed et al., 2021). Their aerodynamic performance depends on factors such as length, pitching amplitude, and frequency. Recent studies have emphasized the concept of the effective angle of attack (He et al., 2020; Sun et al., 2021) over the camber effect hypothesis for explaining lift augmentation. Notably, the time-asymmetric ratio of oscillating TEFs modifies the effective angle of attack, though its specific regularities remain unclear.

The effect of pivot location has also garnered significant attention due to unconventional lifting mechanisms (Mackowski & Williamson, 2017; Fernandez-Feria & Sanmiguel-Rojas, 2020). Tian et al. (2016) experimentally analyzed unsteady vortex features as the pivot location shifted from  $0.16c$  to  $0.52c$ . Li et al. (2019) further investigated the phase lag of lift coefficients across five pivot locations ( $x_p/c = 0, 0.25, 0.5, 0.75, 1$ ), highlighting that pivot location acts as an additional plunging motion. This mechanism was attributed to the lagged development of bound circulation. Additionally, the delayed formation of leading-edge vortices (LEVs) significantly alters vortex dynamics, resulting in a phase lag in aerodynamic forces (Sinha et al., 2021; Seshadri et al., 2023). Despite these insights, implementing movable pivot location schemes remains practically challenging and adds complexity to mechanical systems.

This study investigates the impact of the time-asymmetric ratio of oscillating TEFs and pivot location on aerodynamic performance using a pitching airfoil. Section 2 outlines the problem setup and computational approach

for analyzing the surrounding flow field at high angles of attack. Section 3 presents findings on the influence of the time-asymmetric ratio, ranging from  $\delta = 0$  to  $\delta = 0.4$ , on lift coefficient and flow evolution. The effect of pivot location ( $x_p/c = 0, 0.25, 0.5, 0.75$ ) on vortex dynamics are also analyzed, followed by a discussion on the spatiotemporal cooperative effect of these factors. The concluding remarks are summarized in Section 4.

## 2. PROBLEM SETUP

This section presents numerical validations and a detailed description of the problem. A brief explanation of the numerical method, including the turbulence model, is also provided. In the following section, a sensitivity analysis of the mesh and time step is performed to ensure calculation accuracy.

### 2.1 Theoretical Validity of the Simulations

Shehata et al. (2022) reported that unsteady lift dynamics increased when the trailing edge flap (TEF) oscillated periodically, as observed in experiments. Figure 1(a) illustrates the instantaneous lift coefficient ( $C_L$ ) for a NACA 0012 airfoil at an angle of attack ( $\alpha$ ) of  $10^\circ$ , considering a TEF oscillating amplitude ( $\delta_A$ ) of  $10^\circ$  and a reduced frequency ( $k$ ) of 0.12. It is evident that the periodicity and peak values of the current simulation align with the experimental results; however, significant differences are observed in the trough of the  $C_L$ . A quasi-steady analysis indicates that the mean lift coefficient is approximately 0.5, demonstrating the theoretical validity and relevance of the simulations. These results also confirm the suitability of the SST  $k-\omega$  turbulence model for simulating the oscillating TEFs.

Figure 1(b) compares the present simulation with experimental and other numerical results. The NACA 0012 airfoil, with a chord length of 0.15 m, is assumed to pitch about a fixed pivot located at  $0.25c$ . The angle of attack is represented as a sinusoidal function of time ( $t$ ) given by:

$$\alpha(t) = \alpha_0 + \alpha_m \sin(\omega t) \quad (1)$$

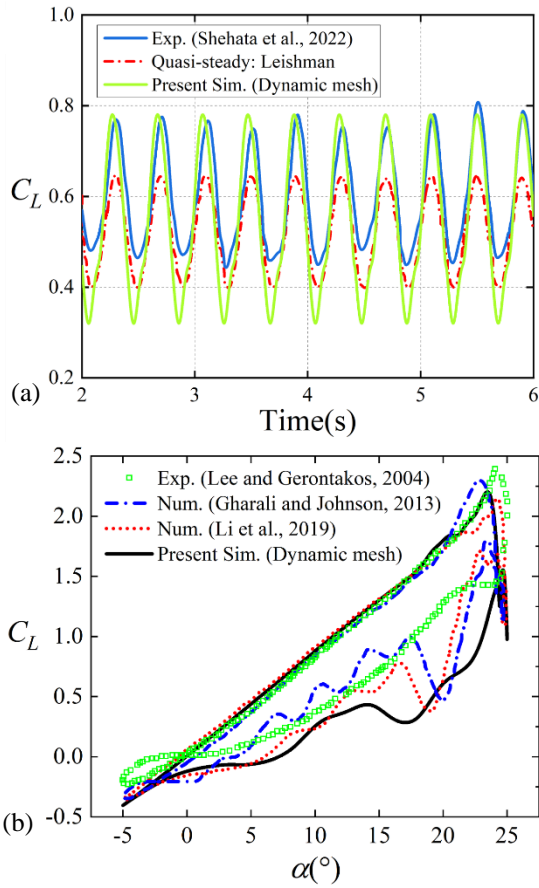


**Fig. 1 Comparison of the present simulation with experimental and other numerical results. (a)  $C_L$  time history of the static airfoil when oscillating TEF, (b)  $C_L$  hysteresis of a pitching airfoil**

where  $\alpha_0 = 10^\circ$ ,  $\alpha_m = 15^\circ$  and  $k = 0.1$ , as reported in previous studies (Lee and Gerontakos, 2004; Gharali & Johnson, 2013; Li et al., 2019). Additionally, the Reynolds number is  $1.35 \times 10^5$ , with a turbulence intensity limited to 0.08%. The overall trends for four  $C_L$  cycles show consistency, despite some differences in detail. These variations can be attributed to serious flow separation or vortex shedding occurring after the stall angle of attack. Computational simulations are inherently influenced by factors such as grid resolution, turbulence models, and time steps. Additionally, accurately measuring surface pressure during deep stall poses significant challenges. Consequently, the present simulations are considered reasonable and reliable.

## 2.2 Geometry and Kinematics

To replicate the wing-flapping motion observed in natural settings, the TEF oscillates periodically while a NACA 0012 airfoil undergoes pitching at a fixed angle of attack,  $\alpha_0 = 10^\circ$ . The time-asymmetric ratio,  $\delta$ , can be expressed by Eq. (2).

$$\delta = \frac{t_d - t_u}{T} \quad (2)$$

where  $t_d$  and  $t_u$  represent the durations of the downward and upward deflection strokes of the TEF, respectively, and  $T$  denotes the duration of an oscillating period.

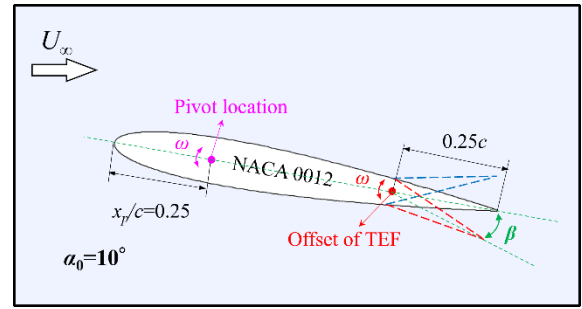


**Fig. 2 Schematic of a pitching airfoil with an oscillating TEF at a fixed pivot location**

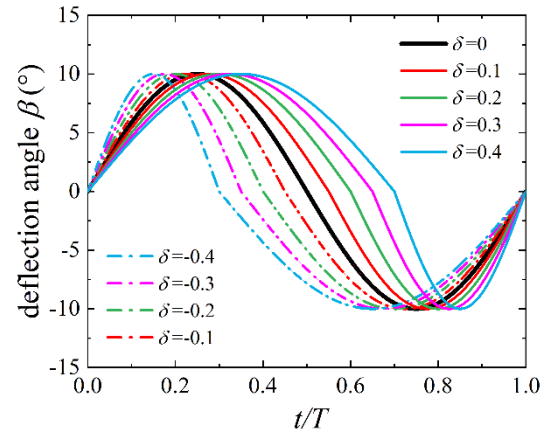


**Fig. 3 Deflection angle of the TEF at varying time-asymmetric ratios  $\delta$**

As shown in Fig. 2, the TEF is hinged at 25% of the chord length from the trailing edge. The dimensionless pivot location is represented as  $x_p/c$  which is the ratio of the distance from the leading edge to the chord length. The default configuration has  $x_p/c = 0.25$ . The kinematic functions governing the oscillating motion of the TEF, in terms of  $\delta$ , are expressed as follows:

$$\beta(t) = \begin{cases} \beta_0 \sin\left(\frac{2\pi f}{1-\delta} t\right), & 0 < t < \frac{1-\delta}{2f} \\ \beta_0 \sin\left(\frac{2\pi f}{1+\delta} t + \frac{2\pi\delta}{1+\delta}\right), & \frac{1-\delta}{2f} < t < T \end{cases} \quad (3)$$

Here, the deflection amplitude,  $\beta_0$ , is  $10^\circ$ , and the  $f$  value conforms to  $k = 0.1$ .

Figure 3 shows the trajectory of the oscillating TEF relative to the main body of the NACA 0012 airfoil. An increase in the time-asymmetric ratio ( $\delta > 0$ ) indicates a faster upward deflection stroke and a slower downward deflection stroke. Conversely, when  $\delta < 0$ , a higher magnitude represents an opposite pattern of oscillatory behavior.

## 2.3 Numerical Method

The flow field generated by the pitching airfoil with an oscillating TEF is governed by the unsteady, incompressible, two-dimensional Navier-Stokes equations, expressed as:

$$\nabla \cdot \mathbf{u} = 0 \quad (4)$$

and

$$\frac{\partial \mathbf{u}}{\partial t} + (\mathbf{u} \cdot \nabla) \mathbf{u} = -\frac{1}{\rho} \nabla p + \nu \nabla^2 \mathbf{u} \quad (5)$$

In the above equations,  $\mathbf{u}$ ,  $t$ , and  $p$  represent velocity, time, and static pressure, respectively. And  $\rho$  and  $\nu$  are air density and kinematic viscosity.

The SST  $k-\omega$  turbulence model is used in the simulations. The exact transport equation for the modified turbulent viscosity is provided in Eq. (6):

$$\begin{aligned} & \frac{\partial}{\partial t}(\rho \tilde{\nu}) + \frac{\partial}{\partial x_i}(\rho \tilde{\nu}_i) \\ & = G_\nu + \frac{1}{\sigma_{\tilde{\nu}}} \left[ \frac{\partial}{\partial x_j} \{ (\mu + \rho \nu) \} + C_{b2} \left( \frac{\partial \tilde{\nu}}{\partial x_j} \right)^2 \right] - Y_\nu + S_{\tilde{\nu}} \end{aligned} \quad (6)$$

On the left side of Eq. (6),  $\tilde{\nu}$  represents the molecular kinematic viscosity. On the right-hand side,  $G_\nu$  and  $Y_\nu$  denote production and destruction terms, respectively, and  $S_{\tilde{\nu}}$  is a user-defined term. The turbulent viscosity is computed as  $\mu = \rho \tilde{\nu} f_{v1}$ , with the terms defined as follows:

$$G_\nu = C_{b1} \rho \tilde{S} \tilde{\nu} \quad (7)$$

$$\tilde{S} = S + \frac{\tilde{\nu}}{\kappa^2 d^2} f_{v2} \quad (8)$$

$$f_{v2} = 1 - \frac{\chi}{1 + \chi f_{v1}} \quad (9)$$

In Eqs. (6) to (9),  $d$  is the distance from the wall, and  $S$  is a scalar measure of the deformation tensor. A modification incorporated into Fluent combines measurements of vorticity and strain tensors, where  $S = |\Omega_j| + 2 \min(0, |S_{ij}| - |\Omega_j|)$ , where  $|\Omega_j| = \sqrt{2\Omega_j \Omega_j}$ , and  $|S_{ij}| = \sqrt{2S_{ij} S_{ij}}$ . The mean strain rate is given as

$$S_{ij} = \frac{1}{2} \left( \frac{\partial u_j}{\partial x_i} + \frac{\partial u_i}{\partial x_j} \right).$$

The viscous damping function  $f_{v1}$  is given by

$$f_{v1} = \frac{\chi^3}{\chi^3 + C_{v1}^3}, \quad \chi = \frac{\tilde{\nu}}{\nu}.$$

$$Y_\nu = C_{w1} \rho f_w \left( \frac{\tilde{\nu}}{d} \right)^2 \quad (10)$$

$$f_w = g \left[ \frac{1 + C_{w3}^6}{g^6 + C_{w3}^6} \right]^{1/6} \quad (11)$$

$$g = r + C_{w2} (r^6 - r) \quad (12)$$

$$r = \frac{\tilde{\nu}}{\tilde{S} \kappa^2 d^2} \quad (13)$$

In Fluent 2021 R2, the default model constants are:

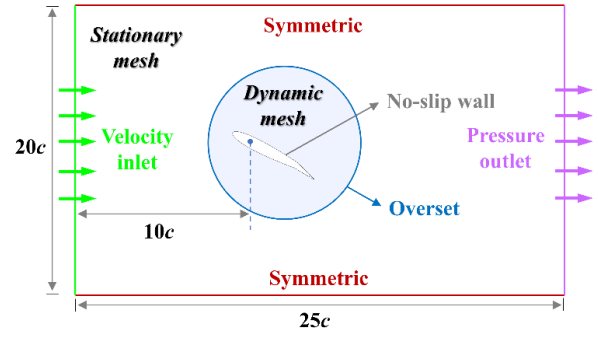


**Fig. 4 A schematic of the computation domain with corresponding boundary conditions**

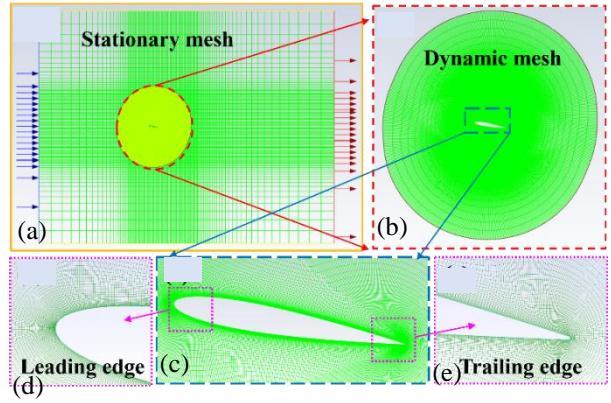


**Fig. 5 Mesh design: (a) Overall mesh, (b) Zoomed view of the overset mesh, (c) Body-fitted mesh around the airfoil, (d) Refined leading edge mesh, (e) Refined trailing edge mesh**

$$C_{w1} = \frac{C_{b1}}{\kappa^2} + \frac{(1 + C_{b2})}{\sigma_{\tilde{\nu}}}, \quad C_{w2} = 0.3, \quad C_{w3} = 2.0, \quad C_{b1} = 0.1355,$$

$$C_{b2} = 0.622, \quad C_{v1} = 7.1, \quad \sigma_{\tilde{\nu}} = \frac{2}{3}, \quad \kappa = 0.4187.$$

Following the setup described by Li et al. (2019), the coupled scheme is employed. The momentum, turbulent kinetic energy, and specific dissipation rate equations are solved using a second-order upwind scheme, with temporal discretization performed using a first-order implicit formulation. Residuals are set to  $10^{-6}$ .

In Fig. 4, the computational domain and boundary conditions are illustrated. The velocity inlet features a uniform free stream  $U_\infty = 14$  m/s at  $10c$  upstream of the original pivot location, and the pressure outlet is located at  $15c$  downstream. Lateral boundaries are symmetric. For the dynamic mesh region, the airfoil surface is defined as a no-slip wall, and the interface condition employs an overset methodology.

Figure 5 illustrates the stationary mesh, which is a structured grid, and the dynamic mesh surrounding the airfoil, constructed using a body-fitted O-block mesh with high surface resolution. The distance between the airfoil surface and the overset boundary is at least  $3c$ . The condition  $y^+ \leq 1$  is maintained to resolve the boundary layer accurately. Flow quantities are coupled between

**Table 1 Sensitivity analysis through spatial and temporal refinements for a pitching airfoil with an oscillating TEF at  $\delta = 0$  and  $x_p/c = 0.25$**

| Cases  | Nodes | $\Delta t$ (s) | $\bar{C}_L$ | $\bar{C}_D$ |
|--------|-------|----------------|-------------|-------------|
| Mesh 1 | 200   | 0.0001         | 0.535       | 0.305       |
| Mesh 2 | 400   | 0.0001         | 0.551       | 0.305       |
| Mesh 3 | 600   | 0.0001         | 0.561       | 0.301       |
| Mesh 4 | 800   | 0.0002         | 0.561       | 0.292       |
| Mesh 3 | 600   | 0.0001         | 0.486       | 0.272       |
| Mesh 3 | 600   | 0.00005        | 0.564       | 0.306       |

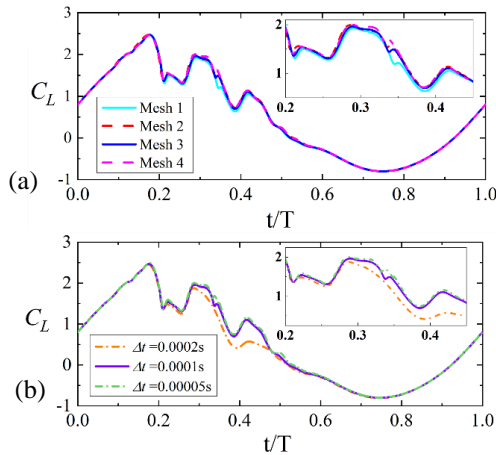


**Fig. 6 Instantaneous  $C_L$  of a pitching airfoil with an oscillating TEF at  $\delta = 0$  and  $x_p/c = 0.25$ : (a) mesh sensitivity, (b) time sensitivity**

stationary and dynamic meshes via interpolation points at the interface boundary. The dynamic mesh technique is applied for prescribed airfoil and TEF motions, controlled by a user-defined function (UDF). However, some small-scale eddies are ignored.

### 2.4 Sensitivity Analysis

Convergence tests were conducted at  $\delta = 0$  and  $x_p/c = 0.25$ . For comparison, four sets of meshes were designed: coarse (Mesh 1), medium (Mesh 2), fine (Mesh 3), and finer (Mesh 4). As shown in Table 1, the averaged lift and drag coefficients exhibited minimal differences across the four meshes and three timesteps. Moreover, Fig. 6(a) illustrates the instantaneous  $C_L$  over one pitching period. The results for Mesh 3 were the most consistent with the curve for Mesh 4. In particular, the violent fluctuations observed in Mesh 3 closely resembled those in Mesh 4, as highlighted in the inset. The  $C_L$  curve for a timestep size of  $\Delta t = 0.0001$  s captured more detailed fluctuations. To balance computational accuracy and cost, Mesh 3 and a timestep size of  $\Delta t = 0.0001$  s were selected for subsequent simulations.

## 3. RESULTS AND DISCUSSION

This section discusses the influence of the time-asymmetric ratio and pivot location on aerodynamic characteristics and analyzes the flow evolution. Both factors control the flow, and it is observed that the spatiotemporal

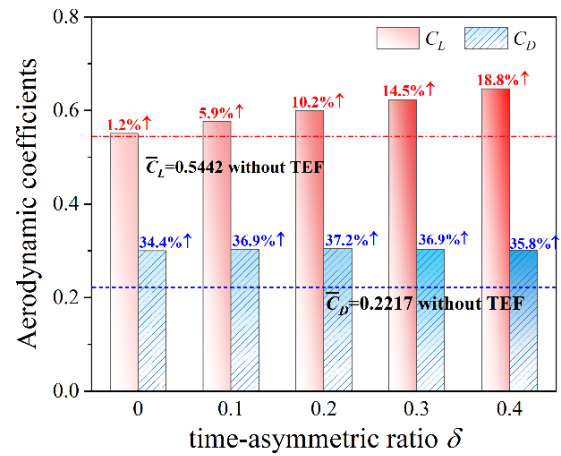


**Fig. 7 Averaged  $C_L$  and  $C_D$  at  $\delta = 0, 0.1, 0.2, 0.3, 0.4$  compared to the case without TEF**

cooperative effect significantly benefits effective flapping flight. In subsection 3.3, new forms of the effective angle of attack are proposed to explain this phenomenon and reveal the underlying flow mechanisms.

### 3.1 Influence of the Time-Asymmetric Ratio

As the time-asymmetric ratio ( $\delta$ ) increases, the averaged lift coefficient ( $\bar{C}_L$ ) and drag coefficient ( $\bar{C}_D$ ) rise relative to the case without TEF, as shown in Fig. 7. The  $C_L$  increment increases progressively from 5.9% to 18.8% in an arithmetic sequence, while the  $C_D$  increment remains approximately 36%. This indicates that a larger time-asymmetric ratio for the oscillating TEF enhances lift during one cycle without significantly increasing drag.

Instantaneous  $C_L$  curves at various  $\delta$  values are shown in Fig. 8(a). The  $C_L$  increases from 0.801 to 1.182 as  $\delta$  increases. Significant lift improvement occurs during the upstroke, with the first peak and the lowest point of  $C_L$  appearing earlier. The increase in the averaged  $C_L$  is attributed to the extended upstroke duration dominated by attachment flow. Additionally, the hysteresis of  $C_L$  versus the angle of attack ( $\alpha$ ) is evident in Fig. 8(b). During the upstroke, the smoothly rising segment of the  $C_L$  curve elevates as  $\delta$  increases, although the amplification gradually diminishes with larger  $\alpha$ . It is observed that monotonically decreasing  $C_L$  phase shifts before the stall angle of attack. During the downstroke, the fluctuating falling segment of the  $C_L$  curve nearly overlaps across all  $\delta$  values. The increase in  $\delta$  introduces a stable phase shift stemming from limited vortex strength compared to the baseline case ( $\delta = 0$ ). At the minimum angle of attack, a larger  $\delta$  causes a smooth transition from the downstroke to the upstroke due to the rapid response of the TEF, which suppresses drastic changes in flow structures.

Pressure distributions at different instants are shown for varying  $\delta$ . The symbols  $\uparrow$  and  $\downarrow$  represent the upstroke and downstroke, respectively. At  $\alpha = 10^\circ \uparrow$ , the pressure coefficient ( $C_p$ ) increases on the upper surface and decreases on the lower surface as  $\delta$  increases (Fig. 9). Pressure contours reveal that pressure regions expand slightly, with minor deformation near the trailing edge as  $\delta$  increases. In contrast, at  $\alpha = 10^\circ \downarrow$  (Fig. 10), the most

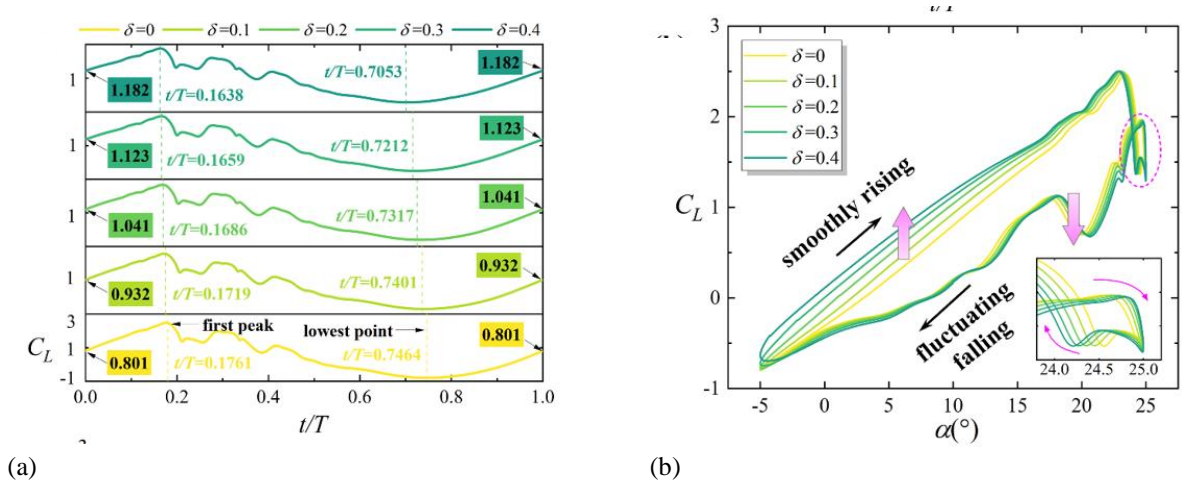


**Fig. 8** Instantaneous  $C_L$  of a pitching airfoil with oscillating TEF at  $\delta = 0, 0.1, 0.2, 0.3, 0.4$  for the fixed pivot location  $x_p/c = 0.25$

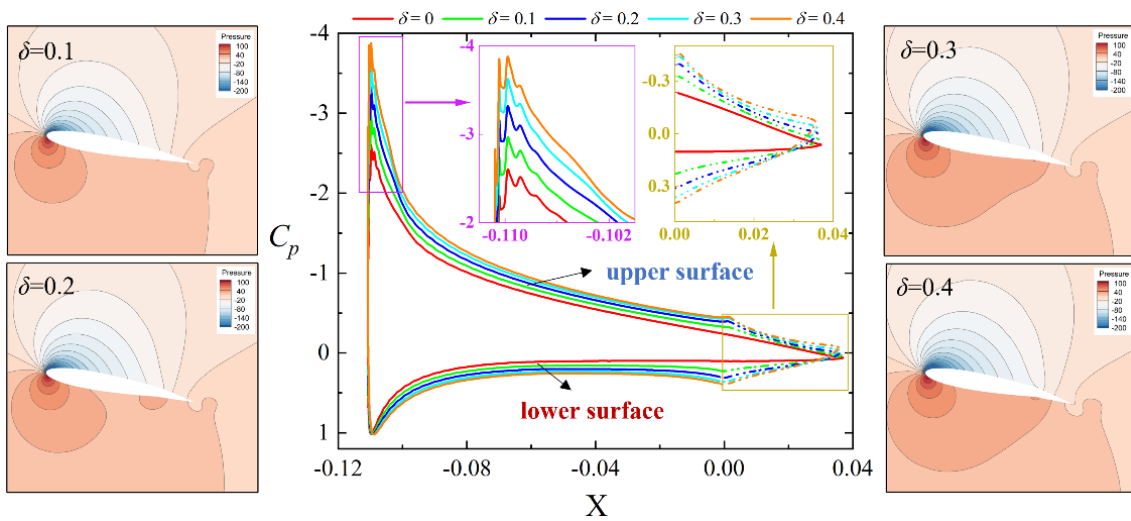


**Fig. 9** Pressure contours and  $C_p$  at  $\alpha = 10^\circ \uparrow$  for different  $\delta$

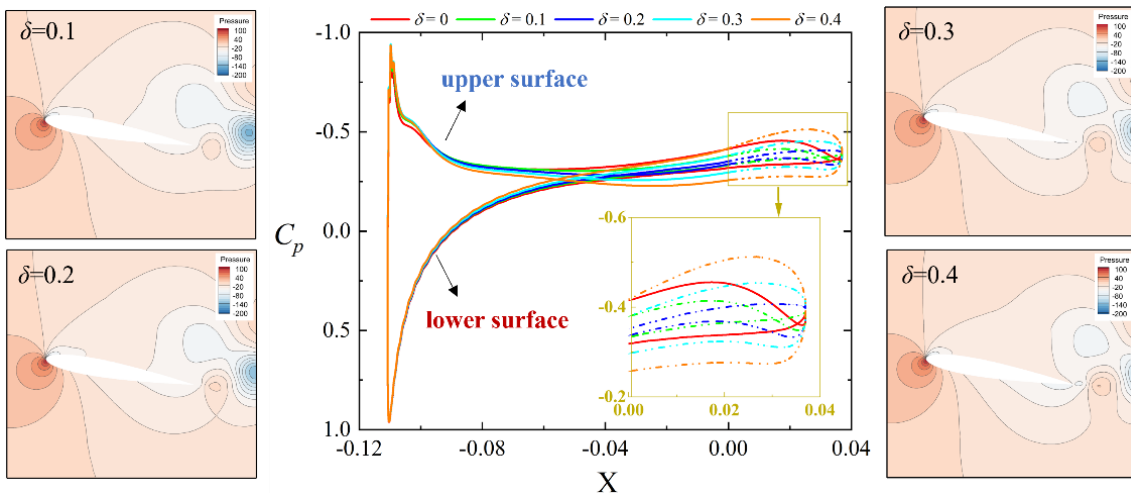


**Fig. 10** Pressure contours and  $C_p$  at  $\alpha = 10^\circ \downarrow$  for different  $\delta$

notable distinction is the dual-loop configuration. The starting position of the reversal curve shifts closer to the leading edge as  $\delta$  increases. The  $C_p$  of the TEF initially decreases and then increases, as shown in the inset image. This behavior arises because the low-pressure region on the upper surface shrinks while the high-pressure region on the lower surface expands with increasing  $\delta$ .

At  $\alpha_{min} = -5^\circ$ , all curves collapse for  $\delta = 0.1$  to  $\delta = 0.4$  (Fig. 11). The  $C_p$  of the TEF shrinks and deforms compared to the  $C_p$  of the leading edge. The high-pressure region is distributed on the lower surface, while an expansive low-pressure region appears on the upper surface. At  $\alpha_{max} = 25^\circ$  (Fig. 12), significant changes in  $C_p$  are observed, particularly for the TEF. The  $C_p$  values on

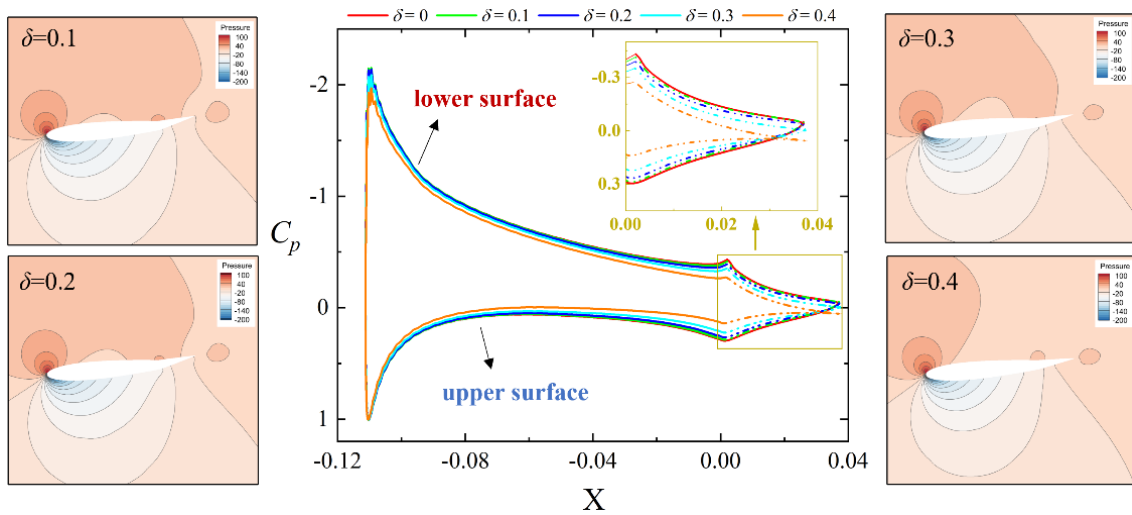


Fig. 11 Pressure contours and  $C_p$  at  $\alpha_{min} = -5^\circ$  for different  $\delta$

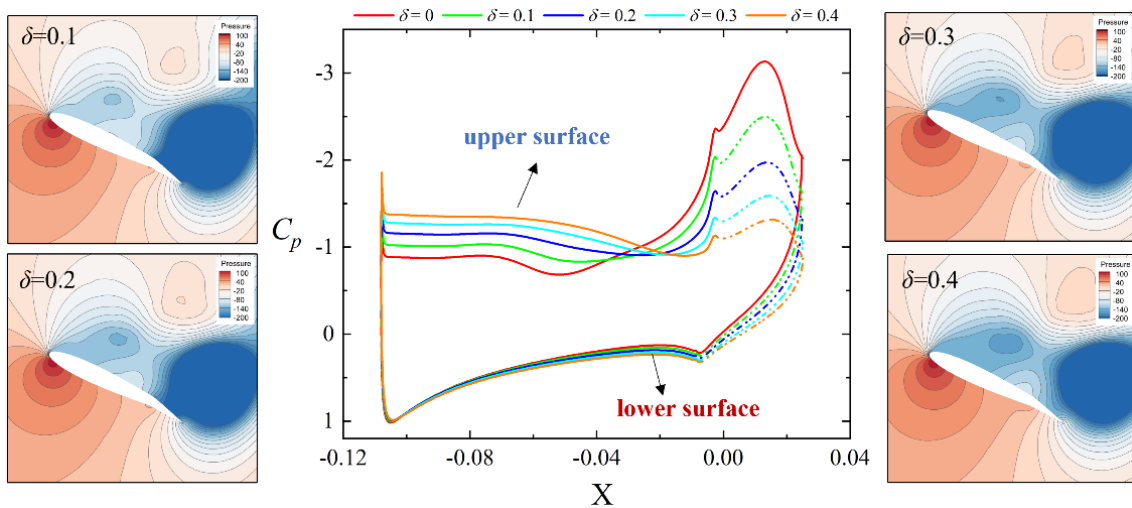


Fig. 12 Pressure contours and  $C_p$  at  $\alpha_{max} = 25^\circ$  for different  $\delta$

the lower surface remain unchanged because the high-pressure regions are similar for all cases. However, the  $C_p$  of the upper surface decreases significantly with increasing  $\delta$ , as low-pressure regions change rapidly and the vortex zone moves away quickly. Additionally, the  $C_p$  of the TEF increases proportionally.

Vortex structures at different instants for  $\delta = 0, 0.1, 0.2, 0.3, 0.4$  are shown in Fig. 13. At  $\alpha = 20.5^\circ \uparrow$ , the first leading-edge vortex (LEV1) gradually grows and moves toward the trailing edge along the upper surface. A clear laminar separation (LS) is observed, preparing to detach, while the first trailing-edge vortex (TEV1) develops. When  $\alpha$  increases to  $22.5^\circ \uparrow$ , LEV1 continues attaching and expanding on the upper surface. Simultaneously, the second leading-edge vortex (LEV2) forms and grows due to the blockage and reverse rotation of the first secondary vortex (SV1), which suppresses LEV1. During the downstroke at  $\alpha = 22.5^\circ \downarrow$ , LEV2 detaches and dissipates downstream, spreading farther as  $\delta$  increases. The third trailing-edge vortex (TEV3) is cut off by the stretching of LEV2, resulting in its rapid dissipation. Subsequently, the second secondary vortex (SV2) and the fourth trailing-edge vortex (TEV4) gradually develop. At  $\alpha = 20.5^\circ \downarrow$ , the

third leading-edge vortex (LEV3) forms while the vestigial vortex filament rolls back to create the returning LEV2 (RLEV2). The RLEV2 invades the space between SV2 and TEV4 due to mutual attraction. Meanwhile, the strength of SV2 diminishes, and TEV4 formation accelerates.

Special vortex structures are shown in Fig. 14. A tertiary vortex (TV) rotates counterclockwise due to the interaction between divided SV1 and TEV2. The generation of TV disrupts the stability of secondary vortices, alleviating stall degree and resulting in a small hysteresis loop as shown in Fig. 8(b). These vortices tend to develop earlier at larger  $\delta$ . The SV2 compresses until it disappears as RLEV2 merges with LEV3 with increasing  $\delta$ . For instance, the TV exists at  $\alpha = 24.85^\circ \uparrow$  for a pitching airfoil without TEF or with oscillating TEF at  $\delta = 0$ , but similar vortex intensity for the TV occurs earlier at  $\alpha = 24.6^\circ \uparrow$  with a larger  $\delta$ . Another observation is the emergence of a reverse trailing-edge vortex (RTEV) when the TEF deflects upward, which shrinks more rapidly at larger  $\delta$ . This indicates that increasing  $\delta$  expedites flow evolution influenced by the real-time TEF dynamics.

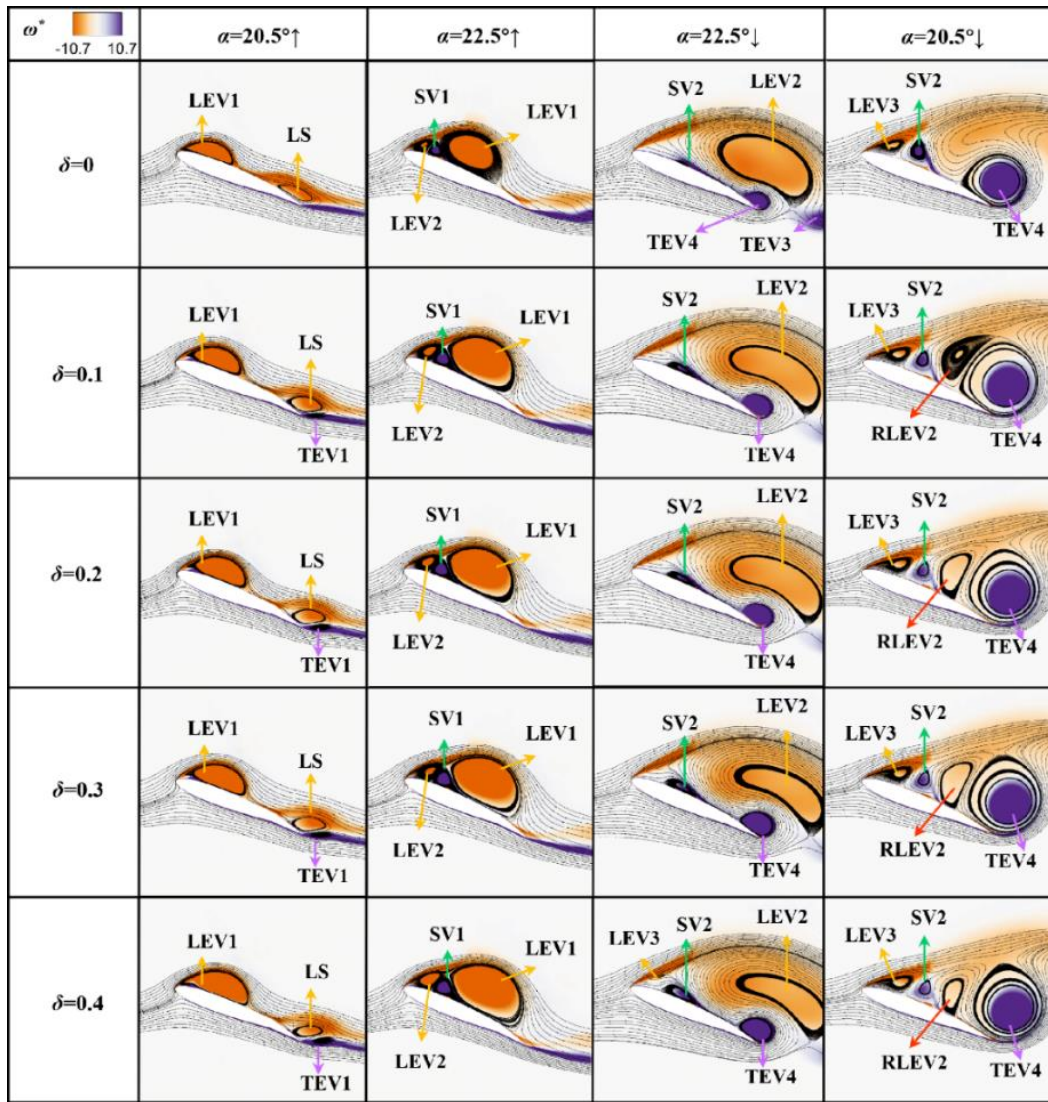


Fig. 13 Vortex structures of a pitching airfoil with oscillating TEF at  $\delta=0, 0.1, 0.2, 0.3, 0.4$  for specific angles of attack in the up- and down-strokes

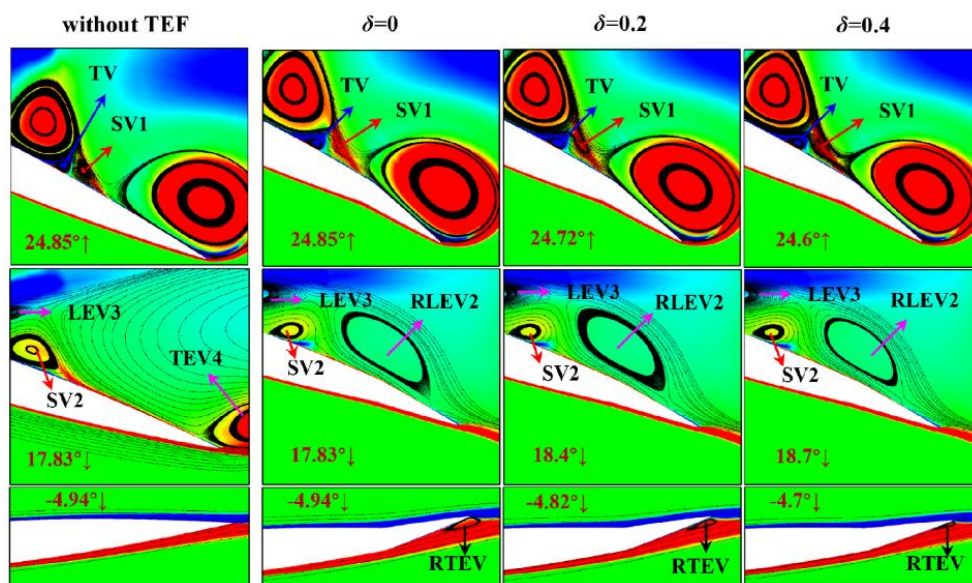
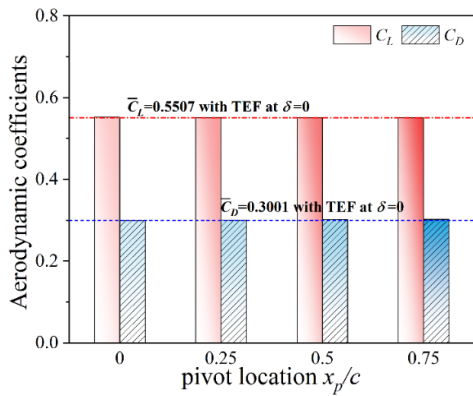


Fig. 14 Special vortex structures for different  $\delta$  compared to the case without TEF



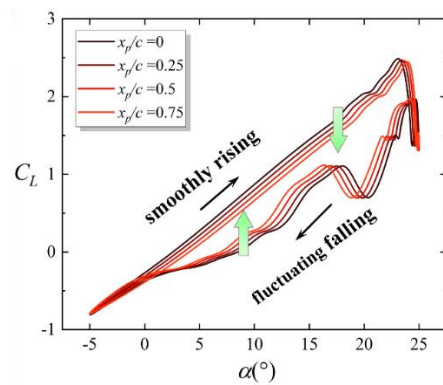
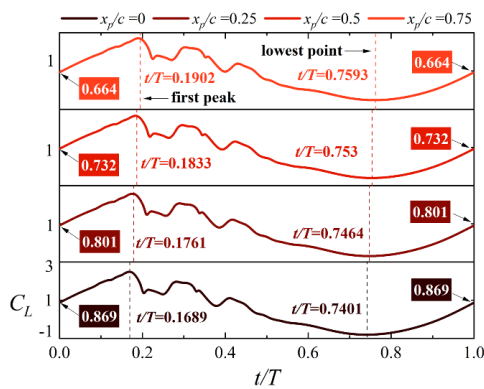
**Fig. 15** Averaged  $C_L$  and  $C_D$  in  $x_p/c = 0, 0.25, 0.5, 0.75$ , compared to those with TEF at  $\delta = 0$

### 3.2 Influence of the Pivot Location

In Fig. 15, the averaged  $C_L$  and  $C_D$  values remain identical across different pivot locations ( $x_p/c = 0, 0.25, 0.5, 0.75$ ) as long as  $\delta = 0$ . It means that the pivot location does not influence the overall aerodynamics within one period when an oscillating TEF is considered.

For the instantaneous  $C_L$  time history, the four curves exhibit complete similarity. As shown in Fig. 16(a), the first peak and lowest point of  $C_L$  occur later as  $x_p/c$  increases, causing the  $C_L$  value to decrease slightly from 0.869 to 0.664 at the beginning of pitching, because attached LEVs develop slower at larger  $x_p/c$ . Figure 16(b) illustrates that the  $C_L$  hysteresis phase remains equivalent during both upstroke and downstroke. Specifically, the smoothly rising segment of  $C_L$  exhibits a modest reduction at the same increasing angle of attack with the backward shift of the pivot location. Conversely, the fluctuating falling segment of  $C_L$  slightly increases at the same decreasing angle of attack. The primary reason is that the backward pivot location likely delays the flow.

Figure 17 presents pressure distributions at different pivot locations ( $x_p/c = 0, 0.25, 0.5$ ). At  $\alpha = 10^\circ \uparrow$ , the maximum pressure difference occurs near the leading edge. Furthermore, as the pivot location moves further backward, the pressure difference decreases. The pressure coefficient ( $C_p$ ) curves for the TEF align well, indicating that the flow remains attached at this stage. Observing the



(a)

(b)

**Fig. 16** Instantaneous  $C_L$  of a pitching airfoil with oscillating TEF in  $x_p/c = 0, 0.25, 0.5, 0.75$  at  $\delta = 0$

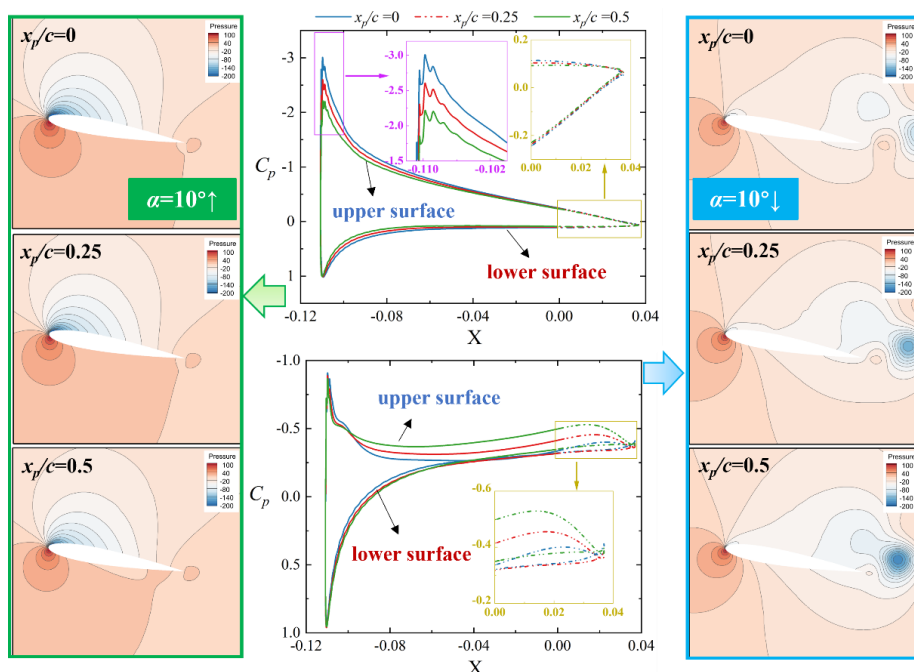


**Fig. 17** Pressure contours and  $C_p$  at  $\alpha = 10^\circ$  during the up- and downstrokes in different  $x_p/c$

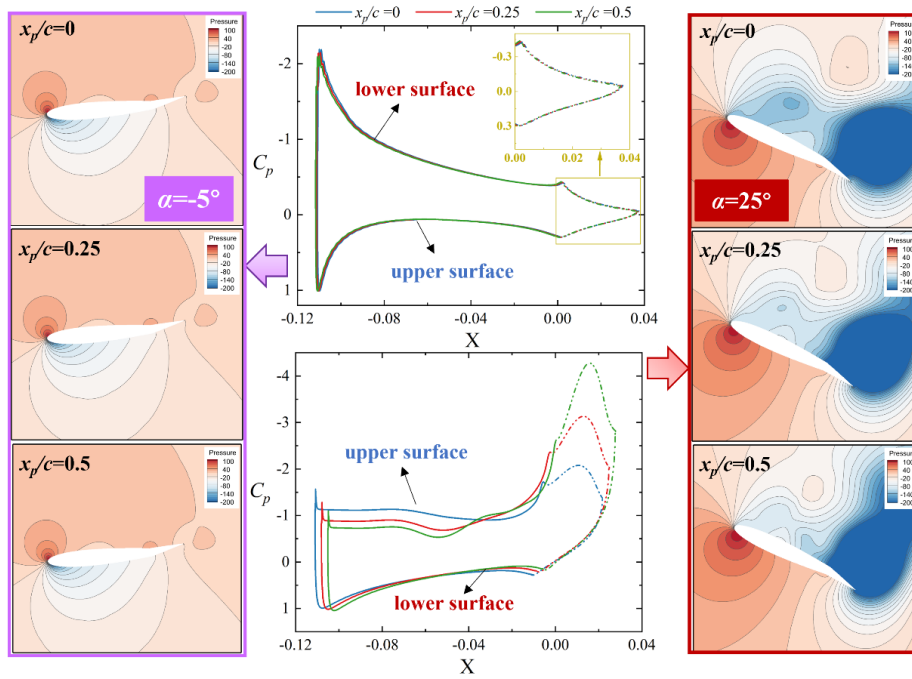


**Fig. 18** Pressure contours and  $C_p$  at  $\alpha_{min} = -5^\circ$  and  $\alpha_{max} = 25^\circ$  in different  $x_p/c$

contours on the left, areas of high-pressure regions shrink as the pivot location moves backward. At  $\alpha = 10^\circ \downarrow$ , the  $C_p$  for the upper surface decreases with increasing  $x_p/c$ , especially for TEF. Additionally, a clear unsteady vortex pattern can be observed in the wake, as shown in the pressure contours on the right. In general, a larger  $x_p/c$  leads to delayed flow evolution, as observed in the vortex region.

In Fig. 18,  $C_p$  of the airfoil at  $\alpha_{min} = -5^\circ$  remains consistent regardless of the pivot location, whereas  $C_p$  at  $\alpha_{max} = 25^\circ$  increases significantly with the increase in  $x_p/c$ . Most notably,  $C_p$  around TEF rises substantially as  $x_p/c$  increases. This is attributed to a large low-pressure region covering the TEF that expands effectively. It can be summarized that delayed flow occurs as the pivot location moves backward, suppressing dynamic stall effectively.

Figure 19 shows that larger  $x_p/c$  tends to induce flow delay. Specifically, LEV1 shrinks, and LS stretches at  $\alpha = 20.5^\circ \uparrow$  as  $x_p/c$  increases. Subsequently, LEV1, LEV2, and SV1 weaken further at  $\alpha = 22.5^\circ \uparrow$ . During the downstroke, deforming LEV2 and TEV3 spread slowly, whereas TEV4 and SV2 undergo compression at  $\alpha = 22.5^\circ \downarrow$  as the pivot location moves backward. At  $\alpha = 20.5^\circ \downarrow$ , TEV4 and SV2 shrink significantly, and the time for RLEV2 formation has not yet been reached.

### 3.3 The Spatiotemporal Cooperative Effect

It can be concluded that increasing  $\delta$  causes the flow to occur earlier, whereas a larger  $x_p/c$  delays the flow. Therefore, it is possible to achieve consistent aerodynamics by comprehensively evaluating these two key factors. In other words, the spatiotemporal cooperative effect between  $\delta$  and  $x_p/c$  has been observed. Figure 20(a) shows the instantaneous  $C_L$  curve for  $x_p/c = 0$ , which nearly coincides with the case at  $\delta = 0.1$ . Based on the vortex details in Fig. 13 and Fig. 19, a high

similarity of RLEV2 is identified at  $\alpha = 20.5^\circ \downarrow$ . Simultaneously, for  $x_p/c = 0.5$ , the pivot location shifts back by  $0.25c$ . At this point, the instantaneous  $C_L$  exhibits a similar trend compared to the case at  $\delta = -0.1$ , as shown in Fig. 20(b).

The angle of attack is a critical parameter in aerodynamic performance studies. Recently, the concept of the effective angle of attack has been widely adopted to explain flow processes and is considered an essential parameter for analyzing the relationship between different motions. When considering only the purely geometric effect of TEF deflection, the effective angle of attack containing  $\delta$  is defined as:

$$\alpha_{eff}^\delta(t) = \alpha(t) + \arctan \left[ \frac{0.25 \sin \beta(t)}{0.75 + 0.25 \cos \beta(t)} \right] \quad (14)$$

Assuming that the movement of the pivot location generates additional plunging motion, an induced angle of attack is immediately produced, accelerating the flow. For  $x_p/c = 0$  and  $0.5$ , the additional plunging motion is given as:

$$h(t) = h_0 \sin(\omega t) \quad (15)$$

where the plunging amplitude is  $h_0 = \pm 0.25c \sin \alpha$ . The induced angle of attack is then described as:

$$\alpha_h(t) = \arctan \left[ \frac{\dot{h}(t)}{U_\infty} \right] \quad (16)$$

Thus, the effective angle of attack at  $\delta = 0$  is defined in the form of Eq. (17).

$$\alpha_{eff}^p(t) = \alpha(t) + \arctan \left[ \frac{0.25 \sin(\beta_0 \sin(\omega t))}{0.75 + 0.25 \cos(\beta_0 \sin(\omega t))} \right] + \alpha_h(t) \quad (17)$$

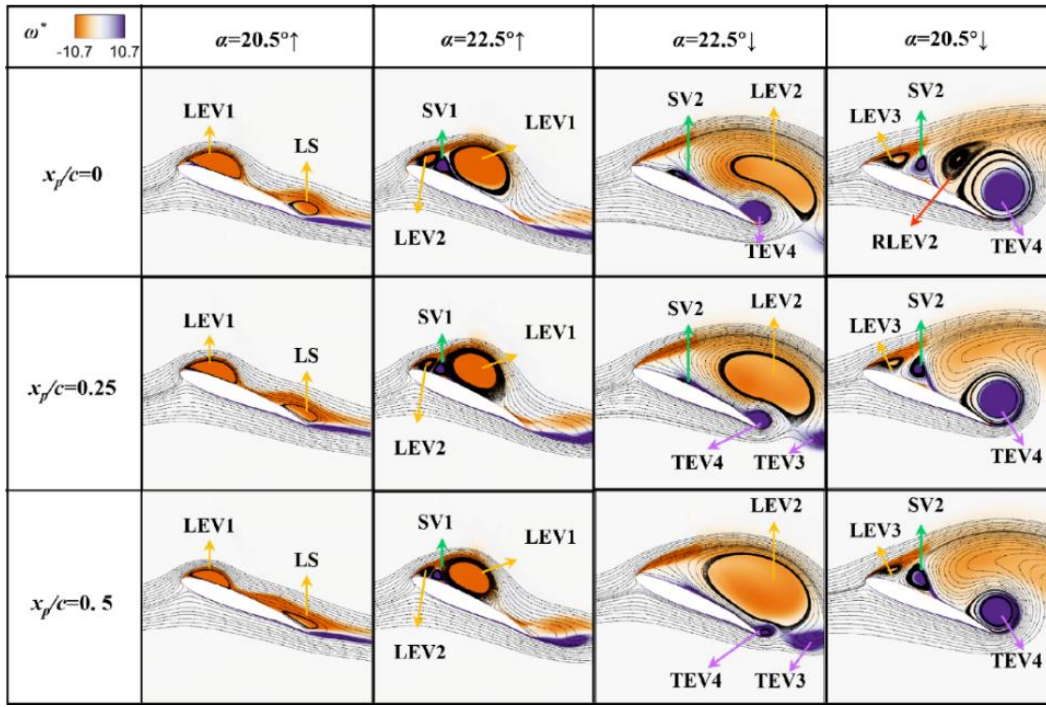


**Fig. 19** Vortex structures of a pitching airfoil with oscillating TEF in  $x_p/c = 0, 0.25, 0.5$  for specific angles of attack in the up- and downstrokes

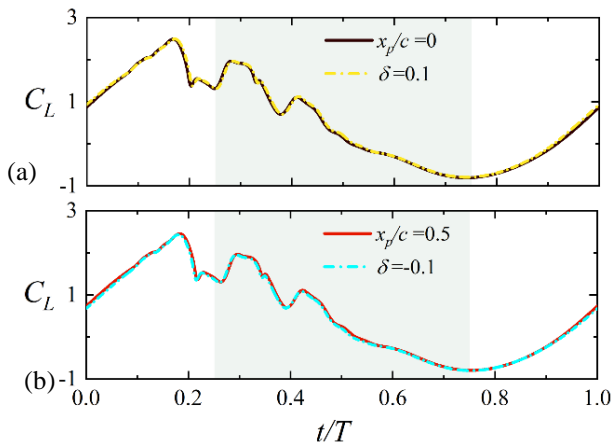


**Fig. 20** Instantaneous  $C_L$  similarity of a pitching airfoil with oscillating TEF: (a)  $x_p/c = 0$  v.s.  $\delta = 0$ . (b)  $x_p/c = 0.5$  v.s.  $\delta = -0.1$ .

For  $\delta = \pm 0.1$ , Eq. (14) closely approximates Eq. (17). As shown in Fig. 21, the two  $\alpha_{eff}$  curves over time are highly similar. The downstroke begins at  $t/T = 0.242$  when the pivot location is forward ( $x_p/c = 0$ ) or  $\delta = 0.1$ , indicating that the flow occurs earlier. However, the downstroke is delayed to  $t/T = 0.259$  when the pivot location shifts backward ( $x_p/c = 0.5$ ) or  $\delta = -0.1$ . It is important to note that the maximum error between the solid and dotted-dashed curves does not exceed 5%. Specifically,  $\delta$  alters the slope of the  $\alpha_{eff}$  curve, while  $x_p/c$  causes a phase shift.

A dimensionless number  $Z$  is defined as:

$$Z = \frac{\omega c \cdot \sin(\alpha_m)}{U_\infty} \quad (18)$$

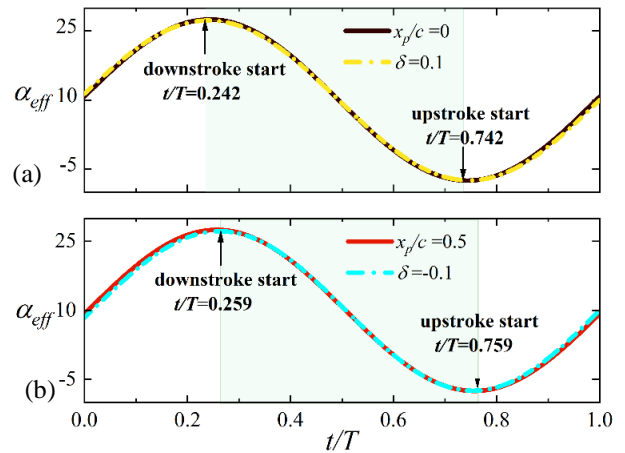


**Fig. 21** The effective angle of attack for two specific cases

This expression is analogous to the tip speed ratio ( $TSR = \frac{\omega R}{v}$ ), where  $Z$  represents the speed ratio of the predominant pitching motion. In this study, the oscillating TEF at  $Z = 0.008$  has a specific length of  $0.25c$  and follows the kinematic equation  $\beta_0 \sin(\omega t)$ . The control parameter  $\delta = \pm 0.1$  plays a similar role to the spatial parameter  $x_p/c = 0.25 \mp 0.25$ . It is speculated that adjusting the time-asymmetry ratio of the oscillating TEF can substitute for the forward or backward movement of the pivot location.

#### 4. CONCLUSION

The effect of the time-asymmetric ratio ( $\delta$ ) of oscillating trailing-edge flaps (TEF) and the pivot location

( $x_p/c$ ) on the lift augmentation of a pitching airfoil at low Reynolds numbers were investigated using a numerical method. The aerodynamic loads and flow evolution for the fixed pivot ( $x_p/c = 0.25$ ) at various  $\delta$  values were first studied. It was observed that the average lift coefficient ( $\bar{C}_L$ ) increased by approximately 17.6% from  $\delta = 0$  to  $\delta = 0.4$ , while the average drag coefficient ( $\bar{C}_D$ ) remained unchanged. The instantaneous lift coefficient  $C_L$  during the upstroke improved significantly at larger  $\delta$  values due to advanced flow development.

The effect of the pivot location  $x_p/c$ , ranging from 0 to 0.75, on flow evolution was also considered. Although the vortex structures exhibited a high degree of similarity, the backward movement of the pivot location resulted in delayed flow evolution. However, this adjustment did not improve the average lift and drag coefficients.

The spatiotemporal cooperative effect between  $\delta$  and  $x_p/c$  is of particular interest. New definitions of the effective angle of attack are introduced to explain the source of the observed aerodynamic characteristics and flow structures. The results indicate that the effective angle of attack ( $\alpha_{eff}^\delta$ ) at  $\delta = \pm 0.1$  is approximately equal to that at  $x_p/c = 0.25 \mp 0.25$  when  $Z=0.008$ . This spatiotemporal cooperative effect suggests that the challenging spatial adjustment of the pivot location can be replaced by temporal parameter control of the oscillating TEF, which is simpler to implement.

This study provides insights into the control of efficient airfoil flapping for high-performance biomimetic aircraft or propulsion systems. It is also relevant for applications in rotorcraft and urban vertical axis wind turbines to improve energy efficiency. However, the quantitative relationship between the time-asymmetric ratio of TEF and the pivot location is derived under constrained conditions and requires further investigation. Moreover, the flow control capability considering the spatiotemporal cooperative effect is limited in enhancing lift.

## ACKNOWLEDGEMENTS

The authors would like to thank supports from Talent Foundation Cooperation Program (Natural Science) of Guizhou University (No. [2022] 46), Basic Research Program (Natural Science) of Guizhou University (No. [2023] 19), Guizhou Provincial Basic Research Programs (No. [2024] Youth 124, No. [2025] General 683) and National Natural Science Foundation of China (No. 52465009).

## CONFLICT OF INTEREST

The authors declare that we have no known competing financial interests or personal relationships that could have appeared to influence the work reported in this paper.

## AUTHORS CONTRIBUTION

**L. Zhu:** Investigation, Writing- original draft. **R. Guo:** Conceptualization, Data Curation, Formal analysis, Funding acquisition, Investigation, Methodology, Project administration, Writing- original draft, Writing- review & editing. **Z. Lai:** Software, Visualization, Writing- review & editing. **L. Qi:** Validation, Funding acquisition. **C. Yin:** Formal analysis, Resources.

## REFERENCES

- Akhter, M. Z., Ali, A. R., & Omar, F. K. (2022). Aerodynamics of a three-dimensional bionic morphing flap. *Sustainable Energy Technologies and Assessments*, 52(D), 102286. <https://doi.org/10.1016/j.seta.2022.102286>
- Akoz, E., Mivehchi, A., & Moored, K. W. (2021). Intermittent unsteady propulsion with a combined heaving and pitching foil. *Physical Review Fluids*, 6(4), 043101. <https://doi.org/10.1103/PhysRevFluids.6.043101>
- Bull, S., Chiereghin, N., Gursul, I., & Cleaver, D. J. (2021). Unsteady aerodynamics of a plunging airfoil in transient motion. *Journal of Fluids and Structures*, 103, 103283. <https://doi.org/10.1016/j.jfluidstructs.2021.103283>
- Chao, L. M., Alam, M. M., & Ji, C. (2021). Drag-thrust transition and wake structures of a pitching foil undergoing asymmetric oscillation. *Journal of Fluids and Structures*, 103, 103289. <https://doi.org/10.1016/j.jfluidstructs.2021.103289>
- Chen, Z., Li, X., & Chen, L. (2022). Enhanced performance of tandem plunging airfoils with an asymmetric pitching motion. *Physics of Fluids*, 34(1), 011910. <https://doi.org/10.1063/5.0079485>
- Elfering, K. H., & Granlund, K. O. (2020). Lift equivalence and cancellation for airfoil surge-pitch-plunge oscillations. *AIAA Journal*, 58(11), 4629–4643. <https://doi.org/10.2514/1.J059068>
- Fernandez-Feria, R., & Alaminos-Quesada, J. (2021). Propulsion and energy harvesting performances of a flexible thin airfoil undergoing forced heaving motion with passive pitching and deformation of small amplitude. *Journal of Fluids and Structures*, 102, 103255. <https://doi.org/10.1016/j.jfluidstructs.2021.103255>
- Fernandez-Feria, R., & Sanmiguel-Rojas, E. (2020). Effect of the pivot point location on the propulsive performance of a pitching foil. *Journal of Fluids and Structures*, 97, 103089. <https://doi.org/10.1016/j.jfluidstructs.2020.103089>
- Gerontakos, P., & Lee, T. (2008). PIV study of flow around unsteady airfoil with dynamic trailing-edge flap deflection. *Experiments in Fluids*, 45(6), 955–972. <https://doi.org/10.1007/s00348-008-0514-4>

- Gharali, K., & Johnson, D. A. (2013). Dynamic stall simulation of a pitching airfoil under unsteady freestream velocity. *Journal of Fluids and Structures*, *42*, 228–244. <https://doi.org/10.1016/j.jfluidstructs.2013.05.005>
- Govindan, S. S., Natarajan, K., & Saini, G. (2023). Active alleviation of fatigue stress on blades by adaptively maneuvered deformable trailing edge flaps (DTEF). *Environmental Science and Pollution Research*, *31*, 39077–39097. <https://doi.org/10.1007/s11356-023-31309-7>
- Hao, F., Tang, T., Gao, Y., Li, Y., Yi, S., & Lu, J. (2021). Continuous morphing trailing-edge wing concept based on multi-stable nanomaterial. *Chinese Journal of Aeronautics*, *34*(7), 219–231. <https://doi.org/10.1016/j.cja.2020.03.041>
- He, G., Deparday, J., Siegel, L., Henning, A., & Mulleners, K. (2020). Stall Delay and Leading-Edge Suction for a Pitching Airfoil with Trailing-Edge Flap. *AIAA Journal*, *58*(12), 5146–5155. <https://doi.org/10.2514/1.J059719>
- Jawahar, H. K., Vemuri, Sh. S., & Azarpeyvand, M. (2022). Aerodynamic noise characteristics of airfoils with morphed trailing edges. *International Journal of Heat and Fluid Flow*, *93*, 108892. <https://doi.org/10.1016/j.ijheatfluidflow.2021.108892>
- Kan, Z., Li, D., Xiang, J., & Cheng, C. (2020). Delaying stall of morphing wing by periodic trailing-edge deflection. *Chinese Journal of Aeronautics*, *33*(2), 493–500. <https://doi.org/10.1016/j.cja.2019.09.028>
- Kim, D. H., & Chang, J. W. (2014). Low-Reynolds-number effect on the aerodynamic characteristics of a pitching NACA0012 airfoil. *Aerospace Science and Technology*, *32*(1), 162–168. <https://doi.org/10.1016/j.ast.2013.08.018>
- Lee, T., & Gerontakos, P. (2004). Investigation of flow over an oscillating airfoil. *Journal of Fluid Mechanics*, *512*, 313–341. <https://doi.org/10.1017/S0022112004009851>
- Li, X., Feng, L. H., & Li, Z. Y. (2019). Flow mechanism for the effect of pivot point on the aerodynamic characteristics of a pitching airfoil and its manipulation. *Physics of Fluids*, *31*(8), 087108. <https://doi.org/10.1063/1.5114833>
- Lu, K., Xie, Y. H., Zhang, D., & Lan, J. B. (2013). Numerical investigations into the asymmetric effects on the aerodynamic response of a pitching airfoil. *Journal of Fluids and Structures*, *39*, 76–86. <https://doi.org/10.1016/j.jfluidstructs.2013.02.001>
- Lu, W., Tian, Y., & Liu, P. (2017). Aerodynamic optimization and mechanism design of flexible variable camber trailing-edge flap. *Chinese Journal of Aeronautics*, *30*(3), 988–1003. <https://doi.org/10.1016/j.cja.2017.03.003>
- Mackowski, A. W., & Williamson, C. H. K. (2017). Effect of pivot location and passive heave on propulsion from a pitching airfoil. *Physical Review Fluids*, *2*(1), 013101. <https://doi.org/10.1103/PhysRevFluids.2.013101>
- Majumdar, D., Bose, C., & Sarkar, S. (2022). Transition boundaries and an order-to-chaos map for the flow field past a flapping foil. *Journal of Fluid Mechanics*, *942*, A40. <https://doi.org/10.1017/jfm.2022.385>
- Mohamed, A., Abdelhady, M., & Wood, D. H. (2021). Using the hinge moment of a trailing edge flap for controlling dynamic stall loads. *Experiments in Fluids*, *62*(9), 184. <https://doi.org/10.1007/s00348-021-03282-9>
- Moriche, M., Flores, O., & Garcia-Villalba, M. (2017). On the aerodynamic forces on heaving and pitching airfoils at low Reynolds number. *Journal of Fluid Mechanics*, *828*, 395–423. <https://doi.org/10.1017/jfm.2017.508>
- Seshadri, P. K., Aravind, A., & De, A. (2023). Leading edge vortex dynamics in airfoils: Effect of pitching motion at large amplitudes. *Journal of Fluids and Structures*, *116*, 103796. <https://doi.org/10.1016/j.jfluidstructs.2022.103796>
- Shehata, H. M., Zakaria, M. Y., Woolsey, C. A., & Hajj, M. R. (2022). Lift enhancement by a flapped trailing edge at low Reynolds number: A frequency response approach. *Journal of Fluids and Structures*, *110*, 103518. <https://doi.org/10.1016/j.jfluidstructs.2022.103518>
- Shi, G., Xiao, Q., & Zhu, Q. (2020). Effects of time-varying flexibility on the propulsion performance of a flapping foil. *Physics of Fluids*, *32*(12), 121904. <https://doi.org/10.1063/5.0027927>
- Sinha, J., Lua, K. B., & Dash, S. M. (2021). Influence of the pivot location on the thrust and propulsive efficiency performance of a two-dimensional flapping elliptic airfoil in a forward flight. *Physics of Fluids*, *33*(8), 081912. <https://doi.org/10.1063/5.0058923>
- Sun, G., Wang, Y., Xie, Y., Ma, P., & Zhang, Y. (2021). Hydrodynamic and energy extraction properties of oscillating hydrofoils with a trailing edge flap. *Applied Ocean Research*, *110*, 102530. <https://doi.org/10.1016/j.apor.2021.102530>
- Thakor, M., Kumar, G., Das, D., & De, A. (2020). Investigation of asymmetrically pitching airfoil at high reduced frequency. *Physics of Fluids*, *32*(5), 053607. <https://doi.org/10.1063/5.0006659>
- Tian, W., Bodling, A., Liu, H., Wu, J. C., He, G., & Hu, H. (2016). An experimental study of the effects of pitch-pivot-point location on the propulsion performance of a pitching airfoil. *Journal of Fluids and Structures*, *60*, 130–142. <https://doi.org/10.1016/j.jfluidstructs.2015.10.014>

Ting, E., Chaparro, D., Nguyen, N., & Fujiwara, G. E. C. (2018). Optimization of variable-camber continuous trailing-edge flap configuration for drag reduction. *Journal of Aircraft*, 55(6), 2217–2239. <https://doi.org/10.2514/1.C034810>

Wang, G., Ng, B. F., Teo, Z. W., Lua, K. B., & Bao, Y. (2021). Performance augmentation mechanism of tandem flapping foils with stroke time-asymmetry.

*Aerospace Science and Technology*, 117, 106939. <https://doi.org/10.1016/j.ast.2021.106939>

Wu, Y., Dai, Y., Yang, C., Hu, Y., & Huang, G. (2023). Effect of trailing-edge morphing on flow characteristics around a pitching airfoil. *AIAA Journal*, 61(1), 160–173. <https://doi.org/10.2514/1.J061055>